IEEE Access
Multidisciplinary | Rapid Review | Open Access Journal

Received December 29, 2020, accepted January 12, 2021, date of publication January 18, 2021, date of current version January 25, 2021.

Digital Object Identifier 10.1109/ACCESS.2021.3052258

Analysis and Design Optimization of V-Shaped Permanent Magnet Vernier Motor for Torque Density Improvement

HAMZA AHMAD, (Graduate Student Member, IEEE), AND JONGSUK RO, (Member, IEEE)
School of Electrical and Electronics Engineering, Chung-Ang University, Seoul 06974, South Korea

Corresponding author: Jongsuk Ro (jongsukro@gmail.com)

This work was supported in part by the Basic Science Research Program through the National Research Foundation of Korea funded by the Ministry of Education under Grant 2016R1D1A1B01008058, and in part by the Human Resources Development of the Korea Institute of Energy Technology Evaluation and Planning (KETEP) grant funded by the Korea Government Ministry of Trade, Industry and Energy, under Grant 20204030200090.

ABSTRACT This paper presents an inner rotor vernier motor featuring the V-shaped permanent magnet (PM) rotor topology; the torque performance of the proposed motor is compared to that of a conventional V-Shaped interior PM motor. The volume of the proposed motor is kept 35% lower than that of the conventional motor. The equations of back electromotive force and reactance are presented, and the air gap flux densities and flux density distributions of both motors are analyzed and compared. A 2D finite element analysis is conducted at three different operating speeds in order to investigate the performance of both motors. The torque components indicate that the proposed motor achieves superior torque performance (i.e., higher average torque and lower torque ripple) at a reduced volume, for the same input current density. Moreover, the torque–current angle characteristic curves at different current densities are obtained and compared. The losses, efficiencies, and power factors of both motors are compared and discussed. Finally, multi-objective optimization of the proposed vernier motor is carried out to further enhance its performance. The results of the analysis prove that the proposed motor achieves better torque density owing to the vernier effect and superior torque performance due to the V-shaped rotor topology.

INDEX TERMS Current angle, efficiency, flux density distribution, harmonics, permanent magnet vernier machine, torque density.

I. INTRODUCTION

Owing to advantages such as a high torque density and a compact mechanical structure, vernier permanent magnet (VPM) motors have attracted significant research interest [1]–[3]. The concept of a vernier motor (VM) was first presented as a reluctance VM approximately 50 years ago [4]. However, as the availability of PM materials became common, great interest grown towards research on PM machines [5]–[7]. Consequently, research on PMVMs commenced approximately 30 years ago [8], [9].

Since then, many topologies of VPM machines have been proposed, such as outer rotor [10], consequent pole [11], dual excitation [12] and dual stator [13]. In [14], Lipo derived detailed characteristic design equations of the surface PM vernier machines, including analytical derivations of back electromotive force (EMF), torque, and power factor. Recently, the work on design optimization of VPM machines for specific practical applications has also been carried out [15].

Although a majority of previous efforts were devoted towards radial flux vernier machines, recent studies have focused on axial flux PM vernier (AFPMV) machines [16]–[19]. In this way the advantage of higher torque density because of axial flux and vernier effect is combined. A few topologies of AFPMV machines have been proposed [20], [21]. Zhao *et al.* [20] proposed a dual stator AFPMV featuring the spoke-type magnets. In [21], a multi-stack flux modulating machine was proposed and compared to its corresponding radial flux machine.

Although VPM motors offer a high torque density, they suffer from a low factor [22], [23]. This problem can be

The associate editor coordinating the review of this manuscript and approving it for publication was Guillaume Parent.

alleviated by using a dual stator structure [13], which yields a high torque density and a good power factor; but the cost of the machine is increased. Furthermore, using long end winding turns with integral slot-distributed windings in conventional VPM machines can result in complications; these long end windings occupy a significant portion of the volume of the machine, thereby the advantage of a higher torque density is remunerated. To resolve this problem, toroidal winding and non-overlapping windings have been employed [24]–[26]; however, for the application of these winding arrangements, modifications in the stator topology are required. In [25], a stator featuring an auxiliary tooth slot structure for the non-overlapping winding arrangement is proposed. Similarly, [26] proposes a dual rotor VPM for the toroidal winding arrangement in order to exploit the dual air gap structure. In [27], core design of VPM machine is investigated considering flux modulation and compared with conventional PM machines. The design accounts for the saturation effect in yoke and teeth of stator.

Thus far, a majority of the research on VPM machines has focused on stator topologies, excitation systems, and winding arrangements. Recently, a few studies on the development of suitable rotor topologies for VPM machines have also been conducted [28]–[30]. A surface PMVM has been proposed as a potential alternative for existing PM motors for variable speed applications [28]. Furthermore, [29] proposes a similar approach of replacing an interior permanent magnet (IPM) machine with a dual stator spoke-type structure. In [30], an outer rotor V-shaped VPM is proposed which reduces flux leakage but the mechanical robustness of motor is compromised because of outer rotor structure.

On the other hand, considerable research on the rotor topologies in IPM machines has been conducted, with the aim of enhancing performance [31]–[39]. For instance, the V-shaped PM rotor topology is commercially being used in electric vehicles such as the Toyota Prius 2004 and 2010 and the Camry 2007 [40]. Reference [39] presents a comparison of a V-shaped IPM machine (VIM) and a surface-mounted PM machine; the results indicate that the VIM has lower eddy current losses and a wider constant power speed range. Moreover, a comparison of a VIM with spoke-type, tangential, and U-shaped topologies indicated that the VIM yielded the highest power factor, highest average torque, and lowest torque ripple, as compared to the other topologies [36].

This study proposes an inner rotor V-shaped IPM vernier motor (VIVM) as a potential alternative to conventional VIMs which are widely used in hybrid electric vehicles. The proposed motor combines the benefits of the V-shaped PM rotor topology and those of VPM motors. The volume of the proposed motor is 35% lower than that of the VIM so that it gives same output torque as conventional VIM at a reduced volume. The torque density is then further improved by employing multi-objective design optimization.

The remainder of this paper is organized as follows: The design specifications and equations defining the circuit parameters of both motors are discussed and compared in Sections II and III. Section IV presents a comparison of the flux density distributions and air gap flux densities of both motors. The torque components, losses, efficiencies, and power factors of both motors are also compared and analyzed in this section. In Section V, the multi-objective optimization of proposed VIVM using genetic algorithm is discussed. Finally, the conclusions of this study are presented in Section VI; the results prove that the proposed motor achieves a superior torque performance at a significantly lower volume, as compared to the conventional one.

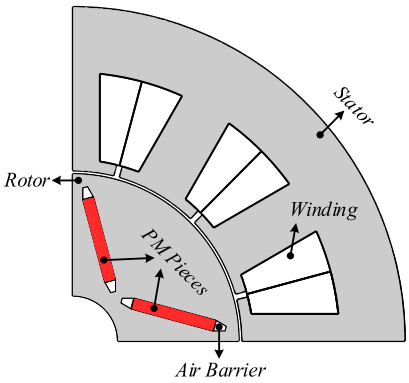

FIGURE 1. Topology of conventional VIM.

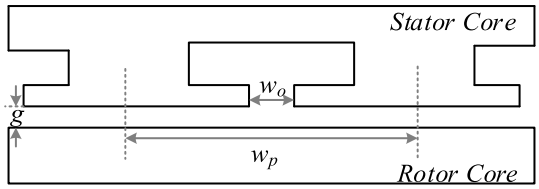

FIGURE 2. Dimensional diagram of conventional VIM.

II. DESIGN OF V-SHAPED CONVENTIONAL IPM MACHINES

To verify the higher torque density and superior torque performance of the proposed VIVM, a widely employed conventional VIM is designed and optimized, for the purpose of a side-by-side design and performance comparison. In [28] and [29], conventional SPM and spoke-type IPM machines, respectively, are compared with proposed VPMs of similar topologies. Hence, a conventional synchronous motor with a V-shaped IPM rotor topology is selected for comparison with proposed VIVM. The geometrical configuration of the motor is presented in Fig. 1. From the figure, it can be seen that the motor has an interior rotor structure; its dimensions are illustrated in Fig. 2, indicating the major design variables associated with the conventional motor. This motor is a 4-pole, 12-slot machine with a distributed full pitch winding. The primary factors influencing design and size, such as the outer radius, current density, and slot fill factor, are identical in both machines for a fair comparison.

As a conventional motor has the same number of rotor and winding poles, a 12-slot, double layer wound machine containing four coils per phase. The number of turns is adjusted according to the slot area in order to achieve the designated current density. The equivalent circuit parameters determine the performance characteristics of the machine. These parameters are expressed in terms of geometrical and winding configurations. As the circuit parameters of a VM differ from those of a conventional motor, it is necessary to compare both these motors. The air gap inductance of the conventional motor, L_{gc}, is expressed as follows:

$$L_{gc} = \frac{\pi \mu_o N^2 L_{stk} D_g}{4 p_c g} = 0.9 k_g \frac{N^2}{p_c^2 g''} \tag{1}$$

where $k_g = (\pi/4)\mu_o L_{stk} D_g$, and p_c & g are the number of winding pole pairs and length of air gap, respectively. D_g, N, and L_{stk} represent the air gap diameter, number of turns per phase, and stack length of the motor, respectively. The air gap reactance expressed in (2) is the product of electrical angular speed and air gap inductance:

$$X_{gc} = \omega_m Z_{rc} L_{gc} = 0.9 c_z k_g \frac{N^2}{p_c g''} \omega_m \tag{2}$$

where ω_m is the mechanical angular speed, and Z_{rc} is the number of rotor pole pairs. The ratio of rotor pole pairs to winding pole pairs is denoted as c_z. The product of the magnetomotive force (MMF) caused by the rotor PMs (3) and the air gap permeance (4) yields the air gap flux density. The back EMF is the integral of the air gap flux density over the coil span; it is expressed in (5). The coefficient B_r is the residual flux of PMs. θ and θ_m are the electrical and mechanical angular displacements, respectively. P_0 and P_1 are constants representing the average and first harmonic of the air gap permeance. Z_{sc} is the number of stator slots in the conventional motor.

$$F_{PM}(\theta, \theta_m) = \frac{4}{\pi} \frac{g_m}{\mu_m} B_r \cos Z_{rc}(\theta - \theta_m) \tag{3}$$

$$P(\theta) = P_0 - P_1 \cos(Z_{sc}\theta) \tag{4}$$

$$E_c = \frac{2\sqrt{2} B_r}{\pi \mu_r} \sin(\frac{\pi}{3}) N D_g L_{stk} \frac{g}{g''} \omega_m f_{\Lambda c} \tag{5}$$

$$f_{\Lambda c} = 1 - 1.6 \beta c_0 \tag{6}$$

The coefficient β expressed in (6) is the ratio of the slot opening width and the air gap length. This relation is nonlinear and ranges from 0 to 0.5. Furthermore, an important factor of comparison between the conventional motor and the VM is c_0, which is the ratio of the slot opening width to the slot pitch.

III. DESIGN OF PROPOSED VIVM

A. OPERATING PRINCIPLE

The geometry of a VM design should combine the rotor pole pairs Z_{rv}, winding pole pairs p_v, stator slot number Z_{sv}, and slots per pole per phase q, as expressed in (7) and (8). For each combination, characteristics of the motor, such as back EMF and air gap reactance, are varied. The vernier effect is a result of the difference between the number of winding pole pairs and the rotor pole pairs. An increase in the number of rotor pole pairs increases the operating frequency of the VM. When designing a VPM, the combination is selected such that the change in geometry, as compared to that of conventional motors, is minimal; this is to ensure that the comparison is fair and valid.

$$Z_{sv} - Z_{rv} = p_v \tag{7}$$

$$Z_{rv} = p_v(6q - 1) \tag{8}$$

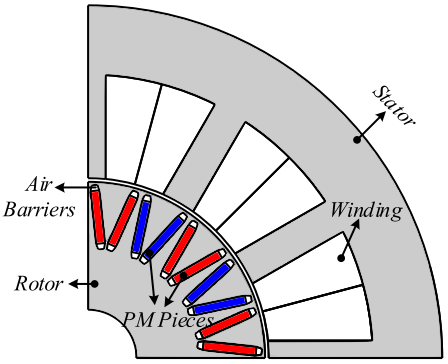

FIGURE 3. Topology of proposed VIVM.

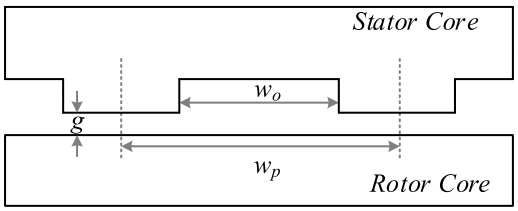

FIGURE 4. Dimensional diagram of proposed VIVM.

B. EQUIVALENT CIRCUIT PARAMETERS

The geometrical configuration in Fig. 3 indicates several poles adjusted in a rotor whose size is identical to that in conventional VIM. Another parameter w_0, which is shown in Fig. 4, is altered to maximize the vernier effect. The stack length is reduced by approximately 35%, without altering the surface area of the motor. The air gap inductance of the VM is expressed in (9). The coefficient of coil pitch α_v is the average of the inner and outer coil pitches; and is due to the concentrated double layer winding. Using (8), the air gap reactance can be obtained as expressed in (10); this obtained value is considerably greater than that of the conventional motor, which is expressed in (2).

$$L_{gv} = \frac{\pi \mu_o N^2 L_{stk} D_g}{4 p_v g} 2\alpha_v (1 - \frac{\alpha_v}{2}) \approx 0.9 k_g \frac{N^2}{p_v^2 g''} \tag{9}$$

$$X_{gv} = \omega_m Z_{rv} L_{gv} = (6q - 1) \frac{N^2}{p_v g''} \omega_m k_g \tag{10}$$

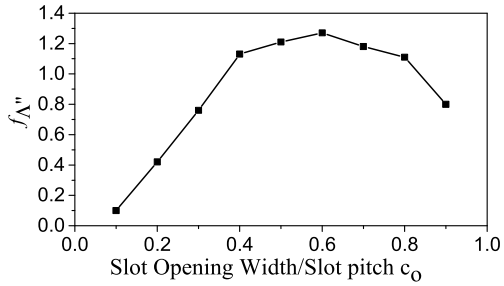

FIGURE 5. Variation of additional flux factor with c_0.

TABLE 1. Detailed design parameters of conventional VIM and proposed VIVM.

Parameter	VIM	VIVM
Pole/Slots	4/12	20/12
Stator outer radius (mm)	46.72	46.72
Rotor outer radius (mm)	23.35	23.35
Air gap length (mm)	0.8	0.8
Stack length (mm)	93	60
Slot area (mm^2)	53.96	78.92
PM material	NdFeB_Br (1.0 T)	NdFeB_Br (1.0 T)
Stator and Rotor Core Material	Steel (50A1000)	Steel (50A1000)
PM thickness (mm)	1.7	1.19
PM volume (mm^3)	15052	15137
PM angle	120	30
Winding type	Y/distributed	Y/concentrated
Turns/phase/coil	196	182
Current density (A/mm^2)	5.5	5.5
Resistance/phase (Ω)	14.08	4.41

The vernier effect arising from the air gap produced by the conditions in (7) and (8) results in an additional flux wave $f_{\Lambda''}$; this wave only depends on the first harmonic of the air gap permeance function, P_1 and is expressed in (11). Hence, an additional factor $f_{\Lambda''}$ is added to the expression of the back EMF of a conventional motor, as shown in (12). This additional flux wave factor is maximized by optimizing the ratio of the slot opening width to the slot pitch, i.e., c_0. Thus, the value of c_0 is selected as 0.6 for this motor. From Fig. 5, it is evident that the maximum value of $f_{\Lambda''}$ is obtained at this point. Finally, the coefficient of the VM f_v is expressed in (13). Detailed design parameters of both the conventional and proposed motors are presented in Table 1. The PM volume of the conventional and proposed motors are almost kept same as can be seen Table 1. Even the number of magnet pieces in VIVM is increased but the length, thickness and depth are considerably reduced, ensuring a negligible difference in the PM volume used for both the motors.

$$f_{\Lambda''} = \frac{6q-1}{\pi}\beta\left(\frac{0.39}{0.39-c_0^2}\right)\sin(1.6c_0\pi) \tag{11}$$

$$E_v = \frac{2\sqrt{2}B_r}{\pi\mu_r}ND_gL_{stk}\frac{2g_{mv}}{g''}\omega_m(f_{\Lambda c}+f_{\Lambda''}) \tag{12}$$

$$f_v = f_{\Lambda c}+f_{\Lambda''} = 1+(3.12q-1.32)\beta \tag{13}$$

The complete design flow of the proposed motor, which is expected to replace conventional IPM machines, is shown in Fig. 6.

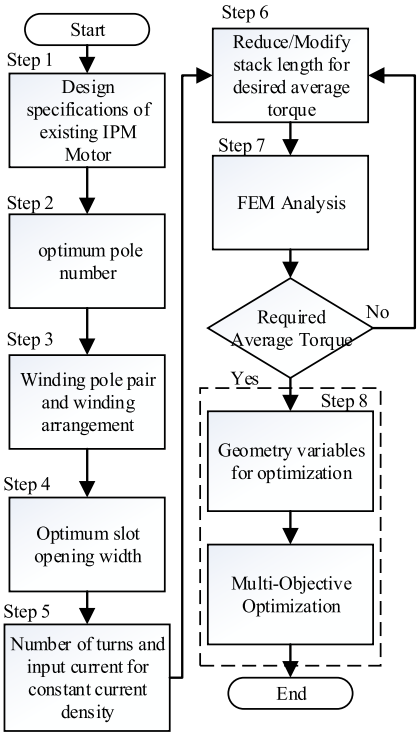

FIGURE 6. Proposed design flow of vernier motor.

Step 1: The design parameters of the conventional motor are obtained and subsequently modified to develop and optimize the design of the proposed VM.

Step 2: An optimal number of rotor poles is selected such that it satisfies (7) and (8). For this purpose, several other parameters, such as PM thickness and angle between PMs, need to be altered, without changing the area of the rotor.

Step 3: The number of winding pole pairs and the number of slots per pole per phase q are selected such that they satisfy (7) and (8). The method of selecting the optimal combination of these parameters has been detailed in [14].

Step 4: As shown in Fig. 5, the vernier effect is maximum at a certain value of c_0. Thus, the slot opening width is modified accordingly.

Step 5: Consequently, the slot area of the motor is altered. Hence, the number of turns is adjusted depending on the slot area and the input current, such that the current density remains identical to that of the conventional motor.

Step 6: The stack length of the motor is reduced to ensure that the torque performance of the designed motor is identical to that of the existing motor.

Step 7: A finite element (FE) analysis is conducted to determine the output average torque. If the output average torque of the proposed motor differs from that of the conventional motor, additional FEM analyses are conducted using a modified stack length.

Step 8: Finally, the optimization variables are selected, and a detailed multi-objective optimization is conducted.

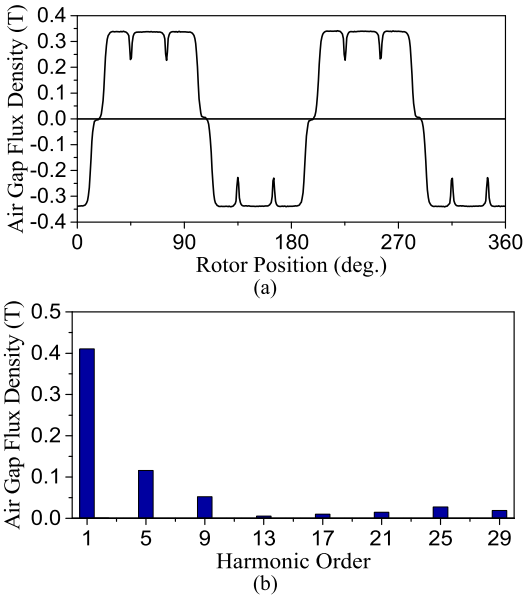

FIGURE 7. Air gap flux density waveform of VIM: (a) air gap flux density waveform and (b) spectral components.

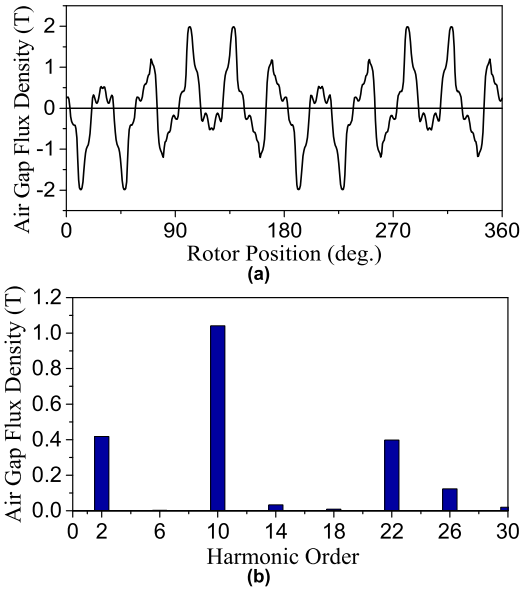

FIGURE 8. Air gap flux density waveform of VIVM: (a) air gap flux density waveform and (b) spectral components.

IV. CHARACTERISTIC ANALYSIS AND COMPARISON OF VIM AND PROPOSED VIVM

A. FLUX DENSITY DISTRIBUTION

The FE analyses of both VIM and the proposed VIVM were performed. The air gap flux density of the VIM is in agreement with that of conventional IPM machines, as shown in Fig. 7(a). The dips in the peak and flat top are attributed to the slotting and fringing effects. The harmonic order in Fig. 7(b) indicates that, besides the fundamental harmonic, the 5th and 9th harmonic orders are considerably significant.

The air gap flux density distribution of the VM differs from that of the conventional IPM machines, because the VM possesses the magnetic gearing effect. The no-load flux density distribution in the air gap of the proposed VIVM is shown in Fig. 8(a). Considering its harmonic order spectrum in Fig. 8(b), it can be seen that the working harmonic order of VIVM corresponds to the number of poles of the machine [41]. Hence the 10th order is the working harmonic order. Besides that, 2nd, 22nd and 26th harmonic orders are significant in torque generation. The other harmonic components, other than the fundamental component, are generated due to the phase modulation of permeance and the MMF generated by the stator windings. Hence, torque in the VIVM is produced via the coupling of the significant harmonic orders with the stator MMF. The magnetic flux density distribution of the VIM under a loaded condition for three operating speeds is analyzed and illustrated, as shown in Fig. 9. It can be seen that the stator yoke and teeth are unsaturated and that the back iron of the stator is completely utilized. However, Fig. 10 depicts that the flux density distribution is considerably lower in the case of the proposed VIVM, even though its winding has the same current density as the conventional motor.

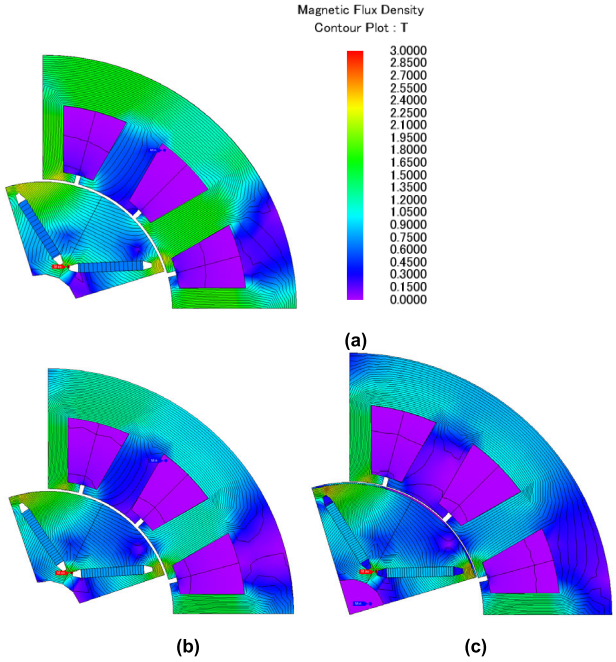

FIGURE 9. Flux density distribution plot of VIM (a) at 360 rpm, (b) 750 rpm, and (c) 1200 rpm.

The strength of the armature reaction decreases significantly because some of the PM flux in the VIVM only circulates in the air gap, without linking the stator windings.

B. BACK EMF

The equivalent back EMFs of the conventional motor and the proposed motor, as discussed in Sections II and III, are expressed in (5) and (12), respectively. The back EMFs of both these motors, which were calculated by conducting FE analyses under no-load conditions, are illustrated in Fig. 11.

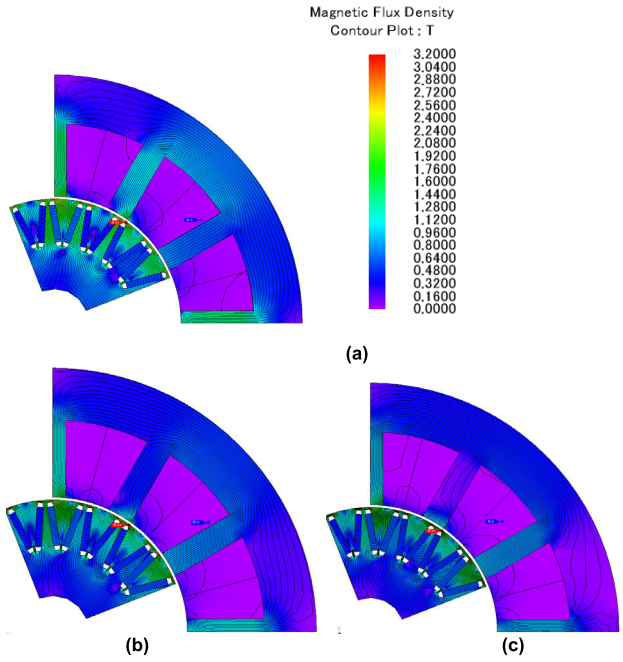

FIGURE 10. Flux density distribution plot of VIVM: (a) at 360 rpm, (b) 750 rpm, and (c) 1200 rpm.

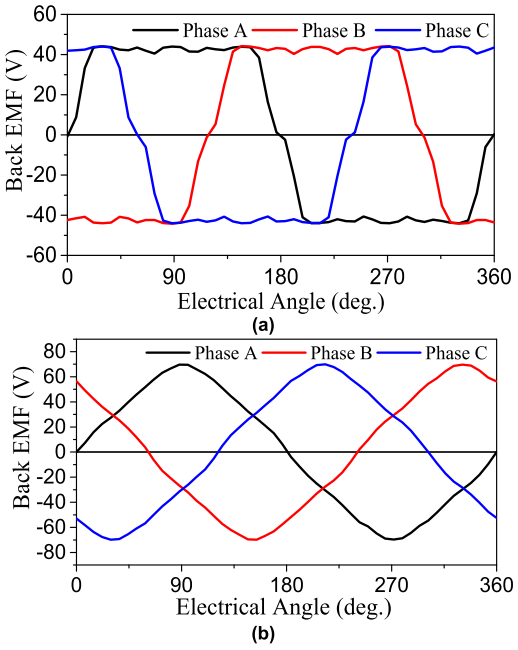

FIGURE 11. Back EMFs at nominal speed of (a) VIM and (b) VIVM.

As shown in the figure, the back EMF of the VIVM is higher than that of the conventional motor, even with the decreased stack length. The corresponding spectral components of both motors are presented in Fig. 12; it is evident that the proposed VIVM features a greater fundamental component as compared to the VIM. Moreover, the 3rd and 5th harmonics of the VM, which result in torque ripples, are also significantly lower than that of the conventional motor.

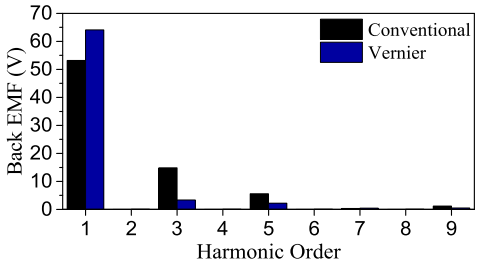

FIGURE 12. Comparison of spectral components of VIM and VIVM.

C. TORQUE RIPPLE AND TORQUE COMPONENTS

Both motors were driven by rated currents at three different operating speeds: 360, 750, and 1200 rpm. The input current is set such that the current densities of both motors remain identical. The cogging torques of both motors are depicted in Fig. 13. As the back EMF of the VIVM yields lower 3rd and 5th harmonics, its cogging torque is significantly lower.

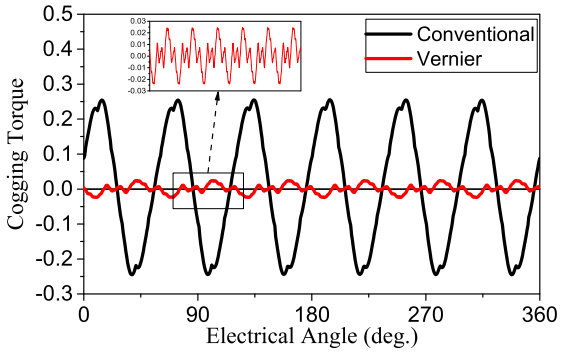

FIGURE 13. Comparison of cogging torques of VIM and VIVM at nominal speed.

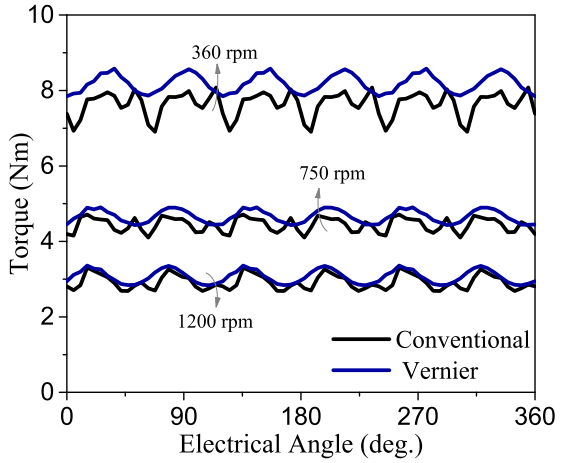

FIGURE 14. Waveforms of torque at different operating speeds.

The output torques of both motors at the abovementioned operating speeds and a current density of 5.5 A/mm^2 are illustrated in Fig. 14. The torque performance of the VIVM with the lower volume is slightly higher than that of the conventional motor. Thus, this motor achieves a higher torque density. The torque ripple of proposed VIVM is also

significantly decreased. The torque ripple of VIVM at all operating speeds is almost half of the torque ripple of VIM. The specific values of the average torque T_{avg} and the torque ripple T_{ripple} for the conventional motor and the proposed motor at all operating speeds are listed in Table 2.

TABLE 2. Torque components of conventional VIM and proposed VIVM.

Operating Speed (rpm)	T_{avg} (Nm)		T_{ripple} (%)	
	VIM	VIVM	VIM	VIVM
360	7.64	8.19	15.4	8.9
750	4.44	4.66	18.2	10.1
1200	2.92	3.06	21.2	12.2

TABLE 3. Torque denisty comparison of conventional and proposed motor.

Torque Density	VIM	VIVM
Nm/m^3	1758321	2921640
Nm/kg	1.56143	2.61146
Nm/kg.m^2	236.183	406.163

From the values of Table 2, the torque density calculated for conventional VIM and proposed VIVM in terms of volume torque (Nm/m^3), mass (Nm/kg) and column torque density (Nm/kg.m^2) is shown in Table 3. The torque density of VIVM is almost 40% more than the conventional VIM.

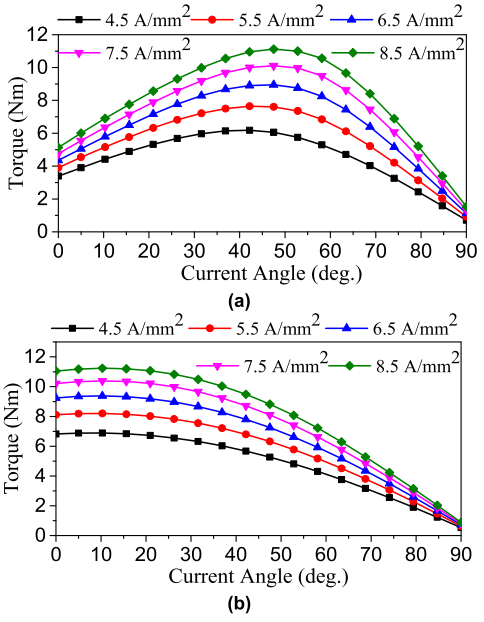

FIGURE 15. Torque vs current angle characteristics of both motors: (a) VIM and (b) VIVM.

The torque–angle characteristics of both machines are shown in Fig. 15. For an air-cooled motor, the allowable current density is 4.5–8.5 A/mm^2. From Fig. 15(a), it is evident that, with an increase in the current density of the VIM, the current angle at which maximum torque is obtained increases by approximately 42°–50°. Moreover, a wide range of the current angle makes it difficult to select an optimal current angle. On the contrary, the current angle characteristic of the VIVM, as shown in Fig. 15(b), remains almost unchanged (at approximately 10°) for all current densities. Hence, the torque constant of the VM remains almost identical even at higher currents; it is not affected by saturation, and the maximum torque can be achieved at different operating points.

D. LOSSES, EFFICIENCY, AND POWER FACTOR

Core losses and iron losses are the primary components of power loss in machines employing PMs. Therefore, these losses in both the motors are compared, as shown in Fig. 16. The iron loss, which is the sum of eddy current losses and core losses, depends on the operating frequency of the drive [14]. As the proposed VIVM has higher number of poles, as compared to the conventional motor, its operating frequency is higher; therefore, its core losses are higher. The copper losses in the proposed motor are also increased by the high-end winding resistance. Moreover, the skin effect and proximity effect also influence this loss at higher frequencies.

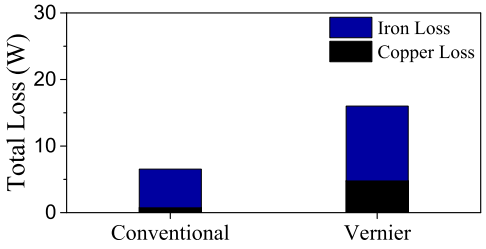

FIGURE 16. Losses of both motors at nominal speed.

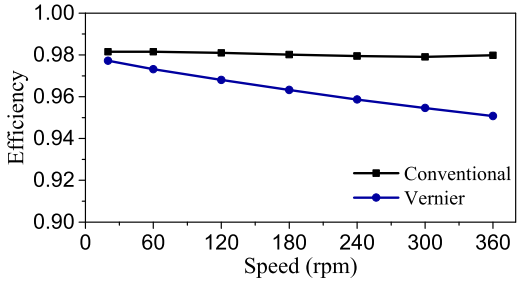

FIGURE 17. Comparison of efficiencies of both motors in constant torque region.

The efficiencies of both motors are calculated, as shown in Fig. 17. The trend of efficiency is observed in the constant torque region. Overall, both the motors exhibit good efficiencies; however, the efficiency of the VIVM is slightly lower than the conventional motor until it reaches the nominal speed. The conventional VIM gives an efficiency of 97.83% while that of proposed motor at nominal speed turns out to be 95.67%. The slight decrease in the efficiency of proposed motor owes to the higher copper and iron losses. This shows that the proposed VIVM is more suitable for the high-torque

low-speed applications because the trade-off of efficiency and torque density will be minimal at lower speeds. A comparison of the power factors of these motors is shown in Fig. 18. It is evident that the VMs inherently suffers from a lower power factor; this is caused by the high frequency of operation, which increases its overall reactance.

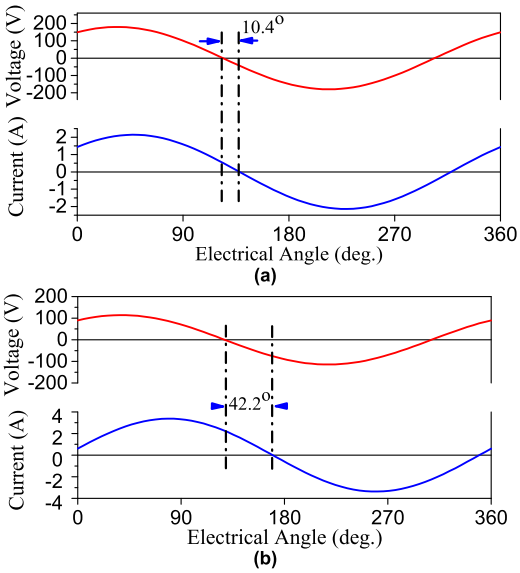

FIGURE 18. Current and voltage waveforms of both motors to obtain power factor angle: (a) VIM and (b) VIVM.

It is noteworthy that even with the lower power factor and decreased efficiency, the advantage of proposed VIVM over conventional VIM in terms of torque density cannot be offset.

E. MECHANICAL STRESS ANALYSIS

In order to insert the PM into the rotor core, it should have a dimensional tolerance between PM and rotor core. The bridges and air-barriers need to be designed carefully considering both mechanical and electromagnetic characteristics. The rotor core should be mechanically robust to operate at high speed. In case of VIM, the PMs are placed well away from the outer edge of rotor so mechanical rotor stresses are not significant and the topology is inherently mechanically stable. However, in case of VIVM the air barriers are close to the rotor edge, hence stress analysis is conducted for it at 1200 rpm. The von-Mises stresses are in Fig. 19 show that the stress levels of VIVM rotor core are well within the allowable limit of 1.5 to 1.9 MPa ensuring that magnets will neither rupture nor fly-off.

V. MULTI-OBJECTIVE OPTIMIZATION OF PROPOSED VIVM

A. VARIABLES FOR OPTIMIZATION

As the initial results of the proposed VIVM are obtained, multi-objective optimization is carried out to further refine the design and maximize its performance. Four key design parameters are chosen which are shown in Fig. 20, where ***YL*** is the yoke length of stator, ***TW*** is the stator tooth width,

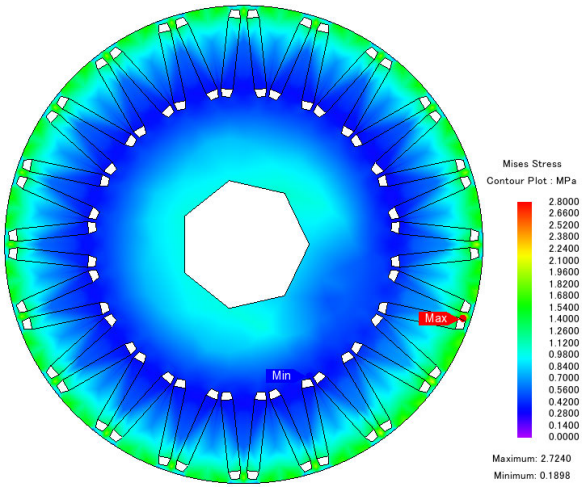

FIGURE 19. Distribution of rotor mechanical stress of VIVM.

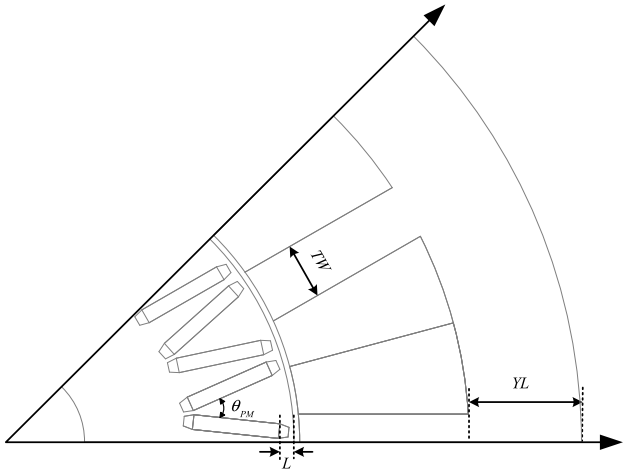

FIGURE 20. Design parameters of VIVM for multi-objective optimization.

$\boldsymbol{\theta_{PM}}$ is the angle between two magnet pieces of same pole and finally $\boldsymbol{L_c}$ is the clearance of magnets from the outer edge of the rotor. To avoid saturation of the motor, these parameters are analyzed individually for the appropriate range for further optimization. In Fig. 21(a)-(d), the relation of optimization variables with output torque is shown in the selected range chosen for optimization. In Fig. 21 (a), the average torque starts decreasing after 30.5° thus the better upper range chosen for $\boldsymbol{\theta_{PM}}$ is 32°. The parameters $\boldsymbol{L_c}$ and ***TW*** have inverse and direct relation with average torque respectively. The optimization range for $\boldsymbol{L_c}$ is 1.27 to 1.87 mm and that of ***TW*** is range 3.5 to 5.5 mm. The effect of ***YL*** as seen in Fig. 21 (c) is not so significant on the output average torque. The range of optimization for this parameter is set from 7 to 11 mm.

B. OPTIMIZATION RESULTS

Multi-objective genetic algorithm (GA) is used for the optimization of VIVM. The population size was set to 40 and

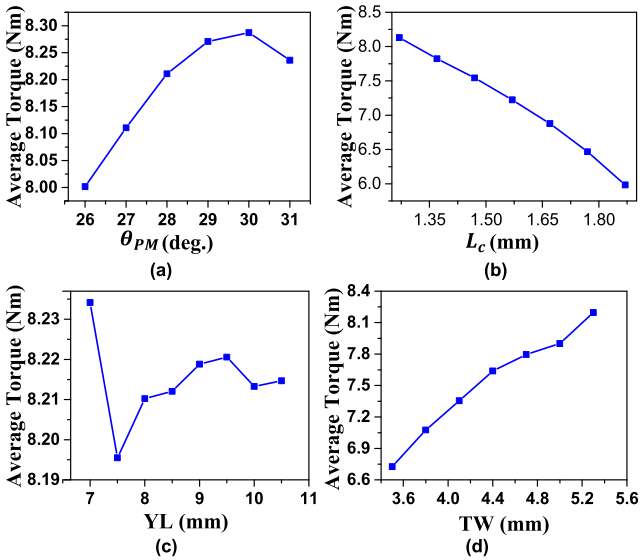

FIGURE 21. Variation of optimization parameters of proposed VIVM. Average Torque VS: (a) PM angle (b) clearance of PM from rotor edge (c) yoke length (d) tooth width.

the number of generations were kept at 25. The objective functions consisted of maximizing the average torque T_{avg} and minimizing the torque ripple T_{ripple}. The optimization results are shown in Fig. 22. The points on the red line are selected as pareto optimal solutions. The model that is chosen as the optimal solution, its corresponding optimized parameters are tabulated in Table 4.

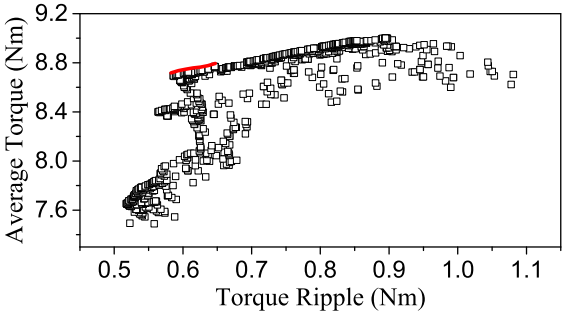

FIGURE 22. Scatter plot with produced feasible solutions in multi-objective GA optimization.

TABLE 4. Optimization parameter values of initial and optimal motor.

Parameter	Initial Values	Optimal Values
PM angle (θ_{PM})	30°	31.86°
PM clearance (L_c)	1.08 mm	1.31 mm
Tooth Width (TW)	4.50 mm	4.87 mm
Yoke Length (YL)	9.15 mm	9.73 mm

In order to verify that the proposed optimized model has improved the overall electromagnetic performance of the VIVM, the performances of the optimal design chosen from

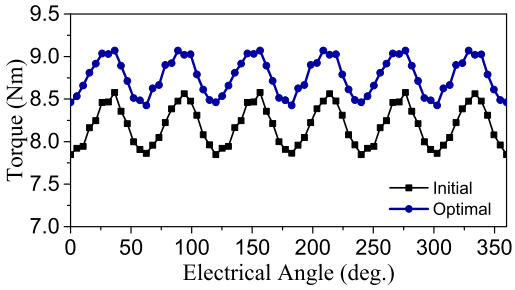

FIGURE 23. Comparison of output torque of initial and optimal motor at 360 rpm.

pareto-optimal front and the initial model are compared. Fig 23 illustrates that the optimal motor can offer higher average torque with the same applied phase current as initial one. The T_{avg} of initial and optimal model are 8.19 and 8.77 Nm respectively. The T_{ripple} of the initial model is 8.9% while that of optimal one is 7.3%. Thus, the optimal motor shows higher average torque and lower torque ripple than the initial motor. The back EMF and power factor of the optimized motor is also slightly increased from the initial motor. The improvement in the torque density of optimal motor is 6.6% from the initial one. The comprehensive comparisons between the initial and optimal VIVM are given in Table 5 where specific values of electromagnetic performance indicators are mentioned. It can be concluded that the optimal motor has significantly increased the average torque and power factor. Besides, the torque ripple is also decreased. Hence, the overall electromagnetic performance of the optimal motor is increased.

TABLE 5. Perfromance comparison of initial and optimal motor.

Parameter	Initial Motor	Optimal Motor
Back EMF (V_{peak})	69	72
Average Torque (Nm)	8.19	8.77
Torque Ripple (%)	8.9	7.3
Losses (W)	18.24	22.19
Efficiency	0.956	0.948
Power Factor	0.740	0.767
Torque Density (Nm/m^3)	2921640	3128530

VI. CONCLUSION

In this paper a VIVM was designed to replace a conventional VIM. The volume of the proposed motor is 35% lower than that of conventional VIM. The performance comparison has been done using FE analysis.

In terms of design, the slot opening width to pitch ratio of the proposed motor is altered to an optimal value of 0.60 to maximize the vernier effects which in turn increases its back EMF. It is found that the proposed VM is capable of achieving a better average torque, even with the 35% lower

volume. The torque ripple of the proposed motor is also halved at all operating speeds. Furthermore, the efficiency of the proposed motor is comparable to that of the conventional motor, with a decrease of just 2% at the nominal speed.

Another advantage of the proposed motor is also evident from its torque–current angle characteristics. Due to smaller variations in the current angle of proposed VIVM, it is easier to select an optimal angle for a wide range of operation with a negligible change in the torque constant.

Multi-objective GA optimization is used to further improve the overall electromagnetic performance of proposed vernier motor. Overall, it was demonstrated that the optimized VIVM offers superior performance with a 44% higher torque density and that it is suitable for replacing conventional IPM motors with V-shaped PM rotor topology which are being used in hybrid electric vehicles. The proposed motor is of key significance for applications such as in-wheel motors where volume reduction of motor is of high priority, without compromising its torque performance.

REFERENCES

[1] R. Qu, D. Li, and J. Wang, "Relationship between magnetic gears and Vernier machines," in *Proc. Int. Conf. Electr. Mach. Syst.*, Beijing, China, Aug. 2011, pp. 1–6.

[2] A. Toba and T. Lipo, "Generic torque-maximizing design methodology of surface permanent-magnet Vernier machine," *IEEE Trans. Ind. Appl.*, vol. 36, no. 6, pp. 2032–2035, Jun. 2005.

[3] S. L. Ho, S. Niu, and W. N. Fu, "Design and comparison of Vernier permanent magnet machines," *IEEE Trans. Magn.*, vol. 47, no. 10, pp. 3280–3283, Oct. 2011.

[4] C. Lee, "Vernier motor and its design," *IEEE Trans. Power App. Syst.*, vol. PAS-82, no. 66, pp. 343–349, Jun. 1963.

[5] S. Madanzadeh, A. Abedini, A. Radan, and J. Ro, "Application of quadratic linearization state feedback control with hysteresis reference reformer to improve the dynamic response of interior permanent magnet synchronous motors," *ISA Trans.*, vol. 99, pp. 167–190, Apr. 2020, doi: 10.1016/j.isatra.2019.08.067.

[6] S. Khan, S. S. H. Bukhari, and J. Ro, "Design and analysis of a 4-kW two-stack coreless axial flux permanent magnet synchronous machine for low-speed applications," *IEEE Access*, vol. 7, pp. 173848–173854, Dec. 2019.

[7] H.-K. Yeo and J. Ro, "Novel analytical method for overhang effects in surface-mounted permanent-magnet machines," *IEEE Access*, vol. 7, pp. 148453–148461, Sep. 2019.

[8] A. Ishizaki, T. Tanaka, K. Takahashi, and S. Nishikata, "Theory and optimum design of PM Vernier motor," in *Proc. 7th Int. Conf. Electr. Mach. Drives*, Durham, U.K., 1995, pp. 208–212.

[9] T. A. Lipo and A. Toba, "Generic torque-maximizing design methodology of surface permanent-magnet Vernier machine," *IEEE Trans. Ind. Appl.*, vol. 36, no. 6, pp. 1539–1546, Nov./Dec. 2000.

[10] J. Li, K. T. Chau, J. Z. Jiang, C. Liu, and W. Li, "A new efficient permanent-magnet Vernier machine for wind power generation," *IEEE Trans. Magn.*, vol. 46, no. 6, pp. 1475–1478, Jun. 2010.

[11] D. Li, R. Qu, J. Li, and W. Xu, "Consequent-pole toroidal-winding outer-rotor Vernier permanent-magnet machines," *IEEE Trans. Ind. Appl.*, vol. 51, no. 6, pp. 4470–4481, Nov./Dec. 2015.

[12] A. Toba and T. A. Lipo, "Novel dual-excitation permanent magnet Vernier machine," in *Proc. Conf. Rec. IEEE Ind. Appl. Conf. 34th IAS Annu. Meeting*, vol. 4, Oct. 1999, pp. 2539–2544.

[13] D. Li, R. Qu, and T. A. Lipo, "High-power-factor Vernier permanent-magnet machines," *IEEE Trans. Ind. Appl.*, vol. 50, no. 6, pp. 3664–3674, Nov./Dec. 2014.

[14] B. Kim and T. A. Lipo, "Operation and design principles of a PM Vernier motor," *IEEE Trans. Ind. Appl.*, vol. 50, no. 6, pp. 3656–3663, Nov./Dec. 2014.

[15] S. Gerber and R.-J. Wang, "Design and evaluation of a PM Vernier machine," in *Proc. IEEE Energy Convers. Congr. Expo. (ECCE)*, Sep. 2015, pp. 5188–5194.

[16] S. Huang, J. Luo, F. Leonardi, and T. A. Lipo, "A comparison of power density for axial flux machines based on general purpose sizing equations," *IEEE Trans. Energy Convers.*, vol. 14, no. 2, pp. 185–192, Jun. 1999.

[17] A. Cavagnino, M. Lazzari, F. Profumo, and A. Tenconi, "A comparison between the axial flux and the radial flux structures for PM synchronous motors," *IEEE Trans. Ind. Appl.*, vol. 38, no. 6, pp. 1517–1524, Nov./Dec. 2002.

[18] D. J. Patterson, J. L. Colton, B. Mularcik, B. J. Kennedy, S. Camilleri, and R. Rohoza, "A comparison of radial and axial flux structures in electrical machines," in *Proc. IEEE Int. Electr. Mach. Drives Conf.*, May 2009, pp. 1029–1035.

[19] A. D. Gerlando, G. Foglia, M. F. Iacchetti, and R. Perini, "Axial flux PM machines with concentrated armature windings: Design analysis and test validation of wind energy generators," *IEEE Trans. Ind. Electron.*, vol. 58, no. 9, pp. 3795–3805, Sep. 2011.

[20] F. Zhao, T. A. Lipo, and B.-I. Kwon, "A novel dual-stator axial-flux spoke-type permanent magnet Vernier machine for direct-drive applications," *IEEE Trans. Magn.*, vol. 50, no. 11, pp. 1–4, Nov. 2014.

[21] L. Li, W. N. Fu, S. L. Ho, S. Niu, and Y. Li, "A quantitative comparison study of power-electronic-driven flux-modulated machines using magnetic field and thermal field co-simulation," *IEEE Trans. Ind. Electron.*, vol. 62, no. 10, pp. 6076–6084, Oct. 2015.

[22] Y. Du, M. Cheng, K. T. Chau, X. Liu, F. Xiao, and W. Zhao, "Linear primary permanent magnet Vernier machine for wave energy conversion," *IET Electr. Power Appl.*, vol. 9, no. 3, pp. 203–212, Mar. 2015.

[23] J. Ji, W. Zhao, Z. Fang, J. Zhao, and J. Zhu, "A novel linear permanent-magnet Vernier machine with improved force performance," *IEEE Trans. Magn.*, vol. 51, no. 8, pp. 1–10, Aug. 2015.

[24] K. Okada, N. Niguchi, and K. Hirata, "Analysis of a Vernier motor with concentrated windings," *IEEE Trans. Magn.*, vol. 49, no. 5, pp. 2241–2244, May 2013.

[25] J. Yang, G. Liu, W. Zhao, Q. Chen, Y. Jiang, L. Sun, and X. Zhu, "Quantitative comparison for fractional-slot concentrated-winding configurations of permanent-magnet Vernier machines," *IEEE Trans. Magn.*, vol. 49, no. 7, pp. 3826–3829, Jul. 2013.

[26] S. Niu, S. L. Ho, W. N. Fu, and L. L. Wang, "Quantitative comparison of novel Vernier permanent magnet machines," *IEEE Trans. Magn.*, vol. 46, no. 6, pp. 2032–2035, Jun. 2010.

[27] B. Kim, "Design of a PM Vernier machine with consideration for modulation flux and comparison with conventional PM motors," *Energies*, vol. 10, no. 11, p. 1819, Nov. 2017.

[28] B. Kim and T. A. Lipo, "Design of a surface PM Vernier motor for a practical variable speed application," in *Proc. IEEE Energy Convers. Congr. Expo. (ECCE)*, Sep. 2015, pp. 776–783.

[29] Z. S. Du and T. A. Lipo, "Torque performance comparison between a ferrite magnet Vernier motor and an industrial interior permanent magnet machine," *IEEE Trans. Ind. Appl.*, vol. 53, no. 3, pp. 2088–2097, May/Jun. 2017.

[30] Y. Chen, X. Zhu, L. Quan, Z. Xiang, Y. Du, and X. Bu, "A V-shaped PM Vernier motor with enhanced flux-modulated effect and low torque ripple," *IEEE Trans. Magn.*, vol. 54, no. 11, pp. 1–4, Nov. 2018.

[31] A. Wang, Y. Jia, and W. L. Soong, "Comparison of five topologies for an interior permanent-magnet machine for a hybrid electric vehicle," *IEEE Trans. Magn.*, vol. 47, no. 10, pp. 3606–3609, Oct. 2011.

[32] G. Pellegrino, A. Vagati, P. Guglielmi, and B. Boazzo, "Performance comparison between surface-mounted and interior PM motor drives for electric vehicle application," *IEEE Trans. Ind. Electron.*, vol. 59, no. 2, pp. 803–811, Feb. 2012.

[33] J. Nerg, M. Rilla, V. Ruuskanen, J. Pyrhonen, and S. Ruotsalainen, "Direct-driven interior magnet permanent-magnet synchronous motors for a full electric sports car," *IEEE Trans. Ind. Electron.*, vol. 61, no. 8, pp. 4286–4294, Aug. 2014.

[34] K. I. Laskaris and A. G. Kladas, "Internal permanent magnet motor design for electric vehicle drive," *IEEE Trans. Ind. Electron.*, vol. 57, no. 1, pp. 138–145, Jan. 2010.

[35] Z. Yang, F. Shang, I. P. Brown, and M. Krishnamurthy, "Comparative study of interior permanent magnet, induction, and switched reluctance motor drives for EV and HEV applications," *IEEE Trans. Transport. Electrific.*, vol. 1, no. 3, pp. 245–254, Oct. 2015.

[36] X. Liu, H. Chen, J. Zhao, and A. Belahcen, "Research on the performances and parameters of interior PMSM used for electric vehicles," *IEEE Trans. Ind. Electron.*, vol. 63, no. 6, pp. 3533–3545, Jun. 2016.

[37] S.-H. Han, W. L. Soong, T. M. Jahns, M. K. Güven, and M. S. Illindala, "Reducing harmonic eddy-current losses in the stator teeth of interior permanent magnet synchronous machines during flux weakening," *IEEE Trans. Energy Convers.*, vol. 25, no. 2, pp. 441–449, Jun. 2010.

[38] K. Yamazaki, M. Kumagai, T. Ikemi, and S. Ohki, "A novel rotor design of interior permanent-magnet synchronous motors to cope with both maximum torque and iron-loss reduction," *IEEE Trans. Ind. Appl.*, vol. 49, no. 6, pp. 2478–2486, Nov./Dec. 2013.

[39] M. Olszewski, "Evaluation of the 2010 Toyota Prius hybrid synergy drive system," U.S. Dept. Energy, Vehicle Technol., Washington, DC, USA, Tech. Rep. 20585-0121, Mar. 2011, pp. 43–48.

[40] P. B. Reddy, A. M. El-Refaie, K.-K. Huh, J. K. Tangudu, and T. M. Jahns, "Comparison of interior and surface PM machines equipped with fractional-slot concentrated windings for hybrid traction applications," *IEEE Trans. Energy Convers.*, vol. 27, no. 3, pp. 593–602, Sep. 2012.

[41] Y. Yu, F. Chai, Y. Pei, and L. Chen, "Comparisons of torque performance in surface-mounted PM Vernier machines with different stator tooth topologies," *IEEE Trans. Ind. Appl.*, vol. 55, no. 4, pp. 3671–3684, Jul./Aug. 2019.

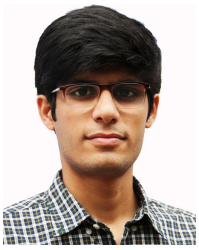

HAMZA AHMAD (Graduate Student Member, IEEE) received the B.S. degree in electrical engineering from the Pakistan Institute of Engineering and Applied Sciences (PIEAS), Pakistan, in 2018. He is currently pursuing the M.S. degree as a Graduate Research Assistant with Chung-Ang University, Seoul, South Korea. His research interests include design and optimization of electrical machines and applications of electromagnetic smart materials.

JONGSUK RO (Member, IEEE) received the B.S. degree in mechanical engineering from Hanyang University, Seoul, South Korea, in 2001, and the Ph.D. degree in electrical engineering from Seoul National University (SNU), Seoul, in 2008. From 2008 to 2012, he conducted research with the Research and Development Center, Samsung Electronics, as a Senior Engineer. From 2012 to 2013, he was with the Brain Korea 21 Information Technology, SNU, as a Postdoctoral Fellow. He conducted research with the Electrical Energy Conversion System Research Division, Korea Electrical Engineering and Science Research Institute, as a Researcher, in 2013. From 2013 to 2016, he worked with the Brain Korea 21 Plus, SNU, as a BK Assistant Professor. In 2014, he joined the University of Bath, Bath, U.K. He is currently an Associate Professor with the School of Electrical and Electronics Engineering, Chung-Ang University, Seoul.